Evidence of zero-point fluctuation of vortices in a very weakly pinned *a*-MoGe thin film

Surajit Dutta [1], Indranil Roy [1], John Jesudasan,[1] Subir Sachdev [2], and Pratap Raychaudhuri [1,*]

[1]*Tata Institute of Fundamental Research, Homi Bhabha Road, Colaba, Mumbai 400005, India*
[2]*Department of Physics, Harvard University, Cambridge, Massachusetts 02138, USA*

In a type-II superconductor, the vortex core (VC) behaves like a normal metal. Consequently, the single-particle density of states in the VC of a conventional type-II superconductor remains either flat or (for very clean single crystals) exhibits a peak at zero bias due to the formation of the Caroli–de Gennes–Matricon bound state inside the core. Here, we report an unusual observation from scanning tunneling spectroscopy measurements in a weakly pinned thin film of the conventional *s*-wave superconductor *a*-MoGe, namely, that a soft gap in the local density of states continues to exist even at the center of the VC. We ascribe this observation to rapid fluctuation of vortices about their mean position that blurs the boundary between the gapless normal core and the gapped superconducting region outside. Analyzing the data as a function of magnetic field, we show that the variation of fluctuation amplitude is consistent with quantum zero-point motion of vortices.

I. INTRODUCTION

In type-II superconductors, the magnetic field penetrates inside the sample above the lower critical field (H_{c1}) in the form of quantized flux tubes called vortices [1], each carrying a magnetic flux of $\Phi_0 = \frac{h}{2e} = 2.07 \times 10^{-15}$ Wb. In the diamagnetic background, the magnetic flux in a vortex is sustained by a circulating supercurrent density (J_s) that falls off inversely with distance from the center of the vortex r as $\mathbf{J}_s \propto 1/r$. The divergence in $\mathbf{J}_s$ as $r \to 0$ is cut off through the formation of a normal metal core at the center of the vortex of the size of the superconducting coherence length ξ. Since the dissipation caused by a moving vortex is contributed by its normal metal core [2], it is of practical interest to understand the electronic structure inside the vortex core (VC). In clean conventional superconductors, the confinement of normal electrons inside the VC gives rise to the formation of bound states of electrons (known as the Caroli–de Gennes–Matricon (CdGM) bound states [3]), which manifest in the form of a peak in the local density of states (LDOS) at Fermi energy E_F. This peak smoothly decays when one moves away from the center of the VC [4–6]. In dirty samples, disorder scattering smears the CdGM peak, eventually leaving a LDOS that is flat over energy scales a few times Δ [7,8]. Consequently, far from the VC, the LDOS exhibits a superconducting gap and coherence peak, whereas inside the core, the LDOS is either flat or exhibits a small peak at zero bias due to the formation of CdGM bound states. While the vast majority of superconductors follow the above description, a handful of superconductors, namely, high-T_c cuprates [9,10] and strongly disordered NbN thin films [11,12], exhibit a radically contrasting behavior. In these systems, inside the VC, the LDOS is neither flat nor shows a zero-energy peak but rather displays a LDOS suppression over an energy scale comparable with the superconducting energy gap. While there is no consensus on the origin of this behavior, in high T_c cuprates, it has been suggested that it is alternatively associated with preformed Cooper pairs [9] or to the presence of a competing order [10]. In strongly disordered NbN thin films, it has been recently suggested [13] that it is associated with the formation of Josephson vortices due to the formation of superconducting puddles induced by strong disorder. However, a third possibility that the vortices are not static but are spatially vibrating about their mean position in the vortex lattice (VL) due to thermal or quantum fluctuations [14–16] has not been considered in this context. As we will explain later, a rapid spatial fluctuation of the vortices will blur the boundary between the regions inside and outside the VC and can also produce a soft gap in the experimentally measured LDOS.

In this paper, we report spectroscopic measurements in the vortex state of a weakly pinned thin film of the amorphous superconductor Mo$_{70}$Ge$_{30}$ (*a*-MoGe) using a low-temperature scanning tunneling microscope (STM). We observe that a soft gap in the LDOS continues to exist in the VC right up to the center of the vortex. Interestingly, *a*-MoGe is a conventional *s*-wave type-II superconductor with no known competing order. Furthermore, the superconducting state for the 20-nm-thick film used in this paper is very homogeneous, as confirmed from scanning tunnelling spectroscopy (STS) maps in zero field, forcing us to look for explanations that have not been considered so far. We show that the magnetic field dependence of the soft gap can be explained if we assume that the vortices spatially fluctuate rapidly about their mean positions. The spatial fluctuation at our lowest temperature of 450 mK is consistent with quantum zero-point fluctuation of vortices, which has been theoretically predicted [15,16] in two-dimensional (2D) superconductors.
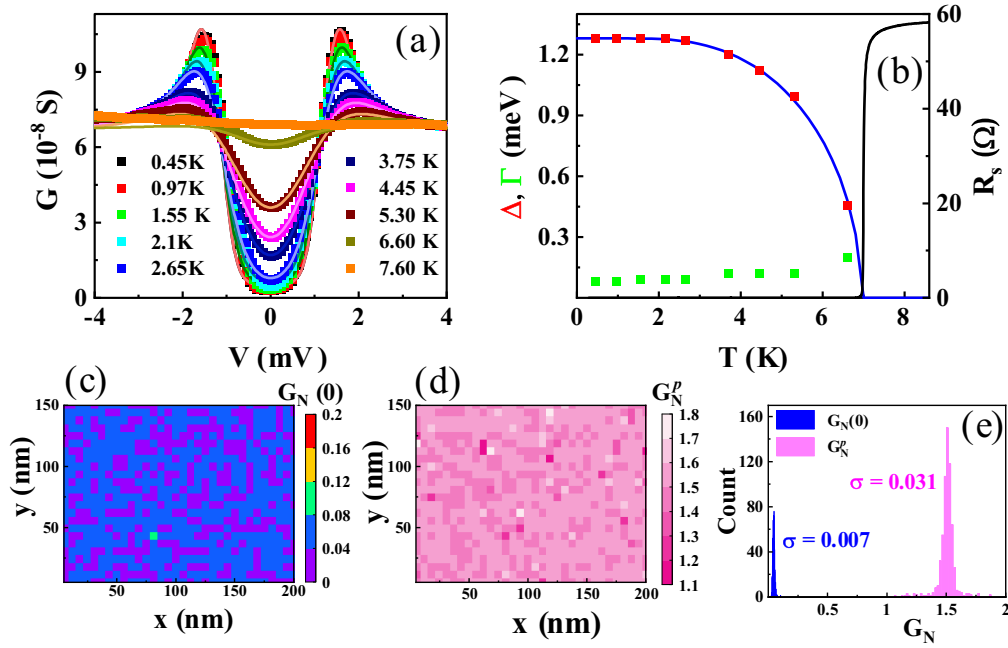
*pratap@tifr.res.in

FIG. 1. (a) $G(V)$-V tunneling conductance spectra in zero field at different temperatures; the solid lines are the fit with Eq. (1). (b) Temperature variation of Δ and Γ obtained from the fits; the temperature variation of R_s is shown in the same panel; the solid blue line is the expected Bardeen-Cooper-Schrieffer (BCS) variation of Δ. Normalized conductance maps at 450 mK at (c) zero bias and (d) bias voltage corresponding to the coherence peak $V^p = 1.45$ mV. (e) Histogram of conductance values $G_N(0)$ and G_N^p, corresponding to panels (c) and (d); the standard deviations (σ) of $G_N(0)$ and G_N^p are shown next to the histograms.

II. SAMPLE AND EXPERIMENTAL DETAILS

The sample used in this paper consisted of 20-nm-thick a-MoGe film like the ones used in Refs. [17–19]. The superconducting transition temperature is $T_c \approx 7.2$ K. Earlier measurements showed that the very weakly pinned 2D VL underwent two structural phase transitions with the magnetic field, from a vortex solid to a hexatic vortex fluid (HVF) and from a HVF to an isotropic vortex liquid (IVL) [17]. As shown before, the films have extremely weak pinning, as evidenced from a very low depinning frequency and the absence of any difference between the field-cooled and zero-field-cooled states [17].

STS measurements were performed in a home-built STM down to 450 mK and fitted with a 90 kOe superconducting solenoid [20]. For STS measurements, after deposition, the film was transferred in the STM using an ultrahigh vacuum suitcase without exposure to air. Measurements were performed using a normal metal Pt-Ir tip. The tip was sharpened *in situ* under high vacuum at 4.2 K using field emission. The sharpness of the tip was verified by acquiring atomic resolution images on an NbSe$_2$ single crystal. The differential

tunneling conductance $G(V)$ was measured by superposing a small AC voltage V_{ac} (150 μV, 2.11 kHz) on the DC bias voltage V_{dc} and measuring the AC current I_{ac} using a lock-in amplifier, so that $G(V = V_{dc}) = dI/dV|_{V=V_{dc}} \approx I_{ac}/V_{ac}$. To image the VL, $G(V)$ maps were recorded with the bias voltage close to the superconducting coherence peak, such that each vortex appears as a local minimum in the conductance. The full $G(V)$-V spectra were recorded by switching off the feedback at a given location and recording $G(V)$ while the bias voltage was swept from positive to negative bias. The time to acquire a complete spectrum was $\sim$2 s. While acquiring full spectroscopic area maps, each spectrum was averaged over three sweeps at every point.

III. RESULTS

We first characterize the zero-field properties of the a-MoGe film using STS. Figure 1(a) shows the average $G(V)$ vs V tunneling spectra, acquired on a 32×24 grid over a 200×150 nm area at different temperatures. The spectra are fitted with the tunneling equation [1]

$$G(V) = \frac{d}{dV}\left\{ \frac{1}{R_N} \int_{-\infty}^{+\infty} N_S(E)N_N(E - eV)[f(E) - f(E - eV)] \right\} dE, \tag{1}$$

where $N_S(E)$ and $N_N(E) \approx 1$ are the normalized densities of states for the superconducting and normal metal, respectively, $f(E)$ is the Fermi-Dirac distribution function, and R_N is the resistance of the tunnel junction for $V \gg \frac{\Delta}{e}$. Here, $N_S(E)$

is given by the Bardeen-Cooper-Schrieffer (BCS) expression $N_S(E) = |\text{Re}[\frac{E - i\Gamma}{\sqrt{(E - i\Gamma)^2 - \Delta^2}}]|$, where Γ is an additional phenomenological parameter [21] which accounts for all
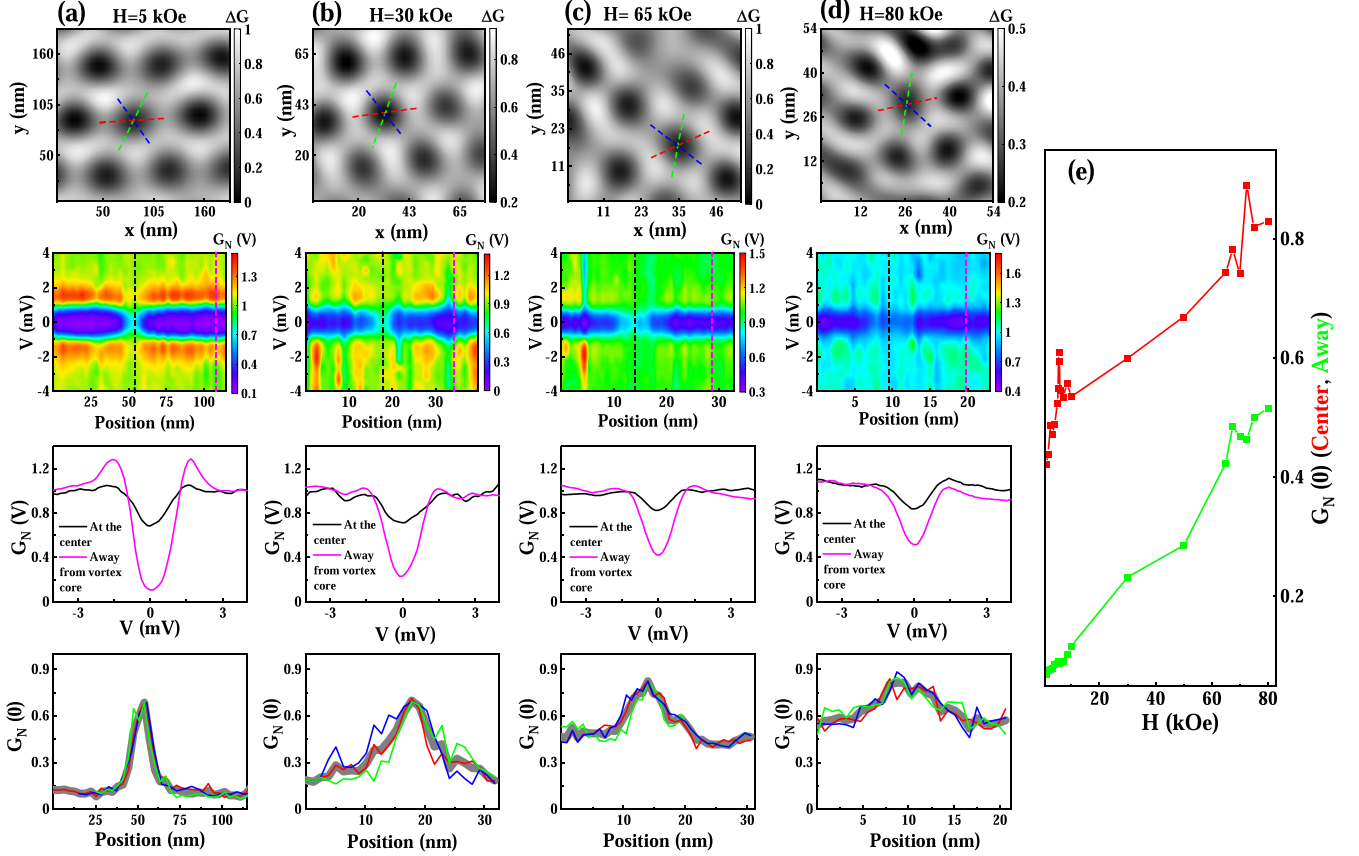
FIG. 2. (a)–(d) The top panels show the image of the vortex lattice over a small area at 450 mK in a field of 5, 30, 65, and 80 kOe, respectively; here, the local variation in conductance ΔG is in arbitrary units. The second row shows the intensity plot of $G_N(V)$ vs V along the red dashed line in the top panel passing through the center of a vortex. The third row shows the spectra at the center of a vortex (black) and at the midpoint between two vortices (Magenta) corresponding to the vertical dashed lines of the same color in the second row. The bottom panels show spatial variation of $G_N(0)$ along the three dashed lines passing through the center of a vortex in the top panel, respectively, along with their average (thick gray line). (e) Variation of $G_N(0)$ with magnetic field at the center of vortices and far from the center.

nonthermal sources of broadening. Figure 1(b) shows the temperature variation of Δ and Γ along with the sheet resistance R_s. Here, $\Delta(T)$ follows the expected BCS variation and goes to zero exactly at the temperature where resistance appears. To produce the conductance maps, we normalize the conductance curve at each point with its value at high bias, i.e., $G_N(V) = \frac{G(V)}{G(6\,\text{mV})}$. In Figs. 1(c) and 1(d), we plot the normalized conductance maps at 450 mK at zero bias $G_N(0)$ and at the bias voltage corresponding to the coherence peak (V^p) averaged for positive and negative voltages $G_N^p = \frac{[G_N(V^p)+G_N(-V^p)]}{2}$. Both the color plots as well as the very small spread in the conductance values observed from the histogram of $G_N(0)$ and G_N^p [Fig. 1(e)] show the homogeneous nature of the superconducting state. This is unlike thinner films that show a large distribution of $G_N(0)$ and G_N^p and the emergence of puddlelike structures [22].

We now turn our attention to the spectroscopy of the VCs (Fig. 2). The top panels of Figs. 2(a)–2(d) show the VL images in different fields at 450 mK over a small area containing 6–8 vortices. Above 5 kOe, the VL enters the hexatic state [17], where defects proliferate in the form of dislocations and locally distort the perfect hexagonal symmetry of the Abrikosov VL. These distortions of the VL affect the supercurrent pattern because of which some vortices, sitting in low-symmetry sites,

appear noncircular in the images at high magnetic fields. The panels in the second row show the normalized conductance spectra $G_N(V)$ vs V along a line passing through the center of a VC. The panels in the third row show representative spectra at the center of the VC and approximately midway between two vortices. Though the superconducting gap starts to fill while approaching the vortex center, a soft gap in the tunneling spectra continues to exist even at the center of the vortex such that $G_N(0) < 1$. The bottom panels show the variation of $G_N(0)$ along three lines passing through the vortex center, as shown by the dashed lines in the top panel. Here, again, we observe that $G_N(0) < 1$ even at the center of the vortex. In Fig. 2(e), we plot $G_N(0)$ at the center of the vortex and at the midpoint between two vortices as a function of magnetic field. We observe that $G_N(0)$ at the center of the vortex shows an overall increasing trend with magnetic field except for two anomalies ~ 5 and 70 kOe. However, the soft gap does not close fully up to 80 kOe.

IV. DISCUSSION

A. Origin of the soft gap inside VC

As mentioned before, the explanations for the soft gap in the VC given for high-T_c cuprates or disordered NbN are

contingent upon the presence of competing order or the presence of strong inhomogeneity in the superconducting state, neither of which are present in our *a*-MoGe film. Furthermore, we do not observe any characteristic feature such as a pseudogap state above T_c which might suggest that the physics of a preformed pair might play any role here. Thus, irrespective of whether those explanations are correct in the context they were proposed, we need to consider a radically different explanation for the soft gap in the VC observed here.

We propose that the soft gap at the center of the vortex arises from rapid spatial motion of the vortices, which vibrate about their mean position. In a solid, which can be visualized as a coupled mass-spring system, such vibrations of atoms arise from two origins: (i) thermal excitations and (ii) quantum zero-point fluctuations. As the solid is cooled, the thermal vibration of atoms gradually decreases, and at low enough temperature, the quantum zero-point fluctuation sets the limiting value of atomic vibration at $T = 0$. For a VL where vortices play the role of atoms, the existence of lattice vibrations has been theoretically postulated [14] even though they have not been experimentally demonstrated. Nevertheless, if we assume that the vortices are spatially vibrating about their mean position, the presence of a soft gap at the center of the vortex can be naturally explained. Since STS is a slow measurement and probes the average tunneling conductance at a given location over time scale of few milliseconds, such rapid fluctuation will get integrated out, thus blurring the boundary between the VC and the gapped superconducting region in between the cores. Therefore, the effect of fluctuation is that the tunneling conductance close to the center of the vortex would have contribution both from the VC as well as regions outside it, thus exhibiting the soft gap.

B. Simulating the conductance maps for fluctuating vortices

We can now explore if the abovementioned physical picture is consistent with our STS data. For that, we need to simulate the conductance map with fluctuating vortices. We start with the simulation of a VL without spatial fluctuations. The exact calculation of the LDOS in the presence of vortices is in principle possible by solving the Usadel equations [23], but this computation is very difficult [24]. Instead, we adopt a simple phenomenological approach like Refs. [25,26]. First, we simulate the regular VL in a superconductor where the vortices are static. We assume that the conductance profile around a vortex can be obtained by interpolating between that at the center of the VC and that far from it. Since in *a*-MoGe the electronic mean free path is very short ($l \approx 0.15$ nm), we assume that, at the center of the VC, the CdGM peak is heavily smeared by disorder scattering [7] such that $G_N(V) = 1$. Far from the core, we assume that the conductance is given by the usual BCS relation given by Eq. (1), $G_N(V) = G_N^{BCS}(T, V, \Delta, \Gamma)$. Here, $G_N^{BCS}(T, V, \Delta, \Gamma)$ is obtained by fitting the experimental zero-field tunneling conductance spectra at the same temperature, with Δ and Γ used as fitting parameters. To simulate the spatial variation of the conductance, we use an interpolation formula of the form

$$G_N(V, \mathbf{r}) = f(\mathbf{r}) + [1 - f(\mathbf{r})]G_N^{BCS}(T, V, \Delta, \Gamma), \quad (2)$$

where $f(\mathbf{r})$ is a position-dependent weight factor. In the absence of a microscopic theory, several authors have proposed different phenomenological forms for $f(\mathbf{r})$ [25,26]. Here, we use a simple Gaussian form $f(\mathbf{r}) = \exp[-\frac{r^2}{2\sigma^2}]$, where σ is of the order of ξ. Numerically, this form produces a variation very similar to the expression in Ref. [26] but introduces fewer adjustable parameters in our eventual analysis. For a VL, the resultant normalized conductance $\tilde{G}_N(V, \mathbf{r})$ is assumed to be a linear superposition of the conductance from all vortices, i.e.,

$$\tilde{G}_N(V, \mathbf{r}) = \frac{\sum_i G_N(V, \mathbf{r} - \mathbf{r}_i)}{\left[\sum_i G_N(V = 0, \mathbf{r} - \mathbf{r}_i)\right]_{max}}, \quad (3)$$

where $\mathbf{r}_i$ is the position of the *i*th vortex and sum runs over all vortices; the normalizing factor ensures that the $\tilde{G}_N(V = 0) = 1$ at the center of each vortex. The consistency of this procedure has been checked by simulating the VL on an NbSe$_2$ single crystal (see Appendix A). Figure 3(a) shows the simulated conductance plots at 10 kOe.

We now take up the situation where the vortices are randomly fluctuating about their mean positions. We assume that the tunneling conductance measured by STS at each point is a temporal average of the instantaneous conductance due to fluctuating vortices. Thus, to simulate the situation when the vortices are randomly fluctuating about their mean positions, we first compute using Eq. (3) the instantaneous conductance map $\tilde{G}_N(V, \mathbf{r}, \Delta a)$ for 200 realizations of a distorted hexagonal lattice with lattice constant a, where each lattice point is displaced by a random vector $\delta \mathbf{r}_i$, satisfying the constraint $|\delta \mathbf{r}_i| \leqslant \Delta a$. Defined in this way, Δa is the amplitude of fluctuations. Each of these 200 realizations corresponds to an instantaneous profile of the conductance. The final simulated conductance profile $G_N^s(V, \mathbf{r}, \Delta a)$ is obtained by taking the average of all 200 realizations, i.e.,

$$G_N^s(V, \mathbf{r}, \Delta a) = \frac{1}{200} \sum_{L=1}^{200} \tilde{G}_N^{(L)}(V, \mathbf{r}, \Delta a) = \langle \tilde{G}_N(V, \mathbf{r}) \rangle_{\Delta a}, \quad (4)$$

where the index L runs over each of the 200 realizations of the distorted lattice. This procedure neglects any retardation effect, which in this context is equivalent to working in the Born-Oppenheimer approximation and is justified if the vibrational frequency of the vortices is much smaller than the gap frequency $\Omega_0 = \frac{2\Delta(0)}{\hbar}$ ($\sim 3.89 \times 10^{12}$ Hz). We will show later that it is the case here.

In Figs. 3(a)–3(d), we show the outcome of these simulations at 10 kOe. Figure 3(a) is for the case of no fluctuation, i.e., $G_N^s(V, \mathbf{r}, \Delta a = 0) \equiv \tilde{G}_N(V, \mathbf{r})$, whereas Figs. 3(b)–3(d) are for increasing magnitude of fluctuations. The top panels show the spatial variation of $G_N^s(V = 0, \mathbf{r}, \Delta a)$ at 10 kOe. The second row shows the corresponding conductance maps at the coherence peak voltage $G_N^s(V^p, \mathbf{r}, \Delta a)$. In the third row, we plot the variation of $G_N^s(0, \mathbf{r}, \Delta a)$ and $G_N^s(V^p, \mathbf{r}, \Delta a)$ along a line passing through the center of the VC. At the center of the core ($x = 0$), the $G_N^s(0, \mathbf{r}, \Delta a)$ progressively decreases from one with increase in $\Delta a/a$; at the same time, $G_N^s(V^p, \mathbf{r}, \Delta a)$ remains >1, showing incomplete suppression of the coherence peak. In the bottom panels, we show the simulated tunneling conductance spectra at the center of a vortex and at the midpoint between two vortices.
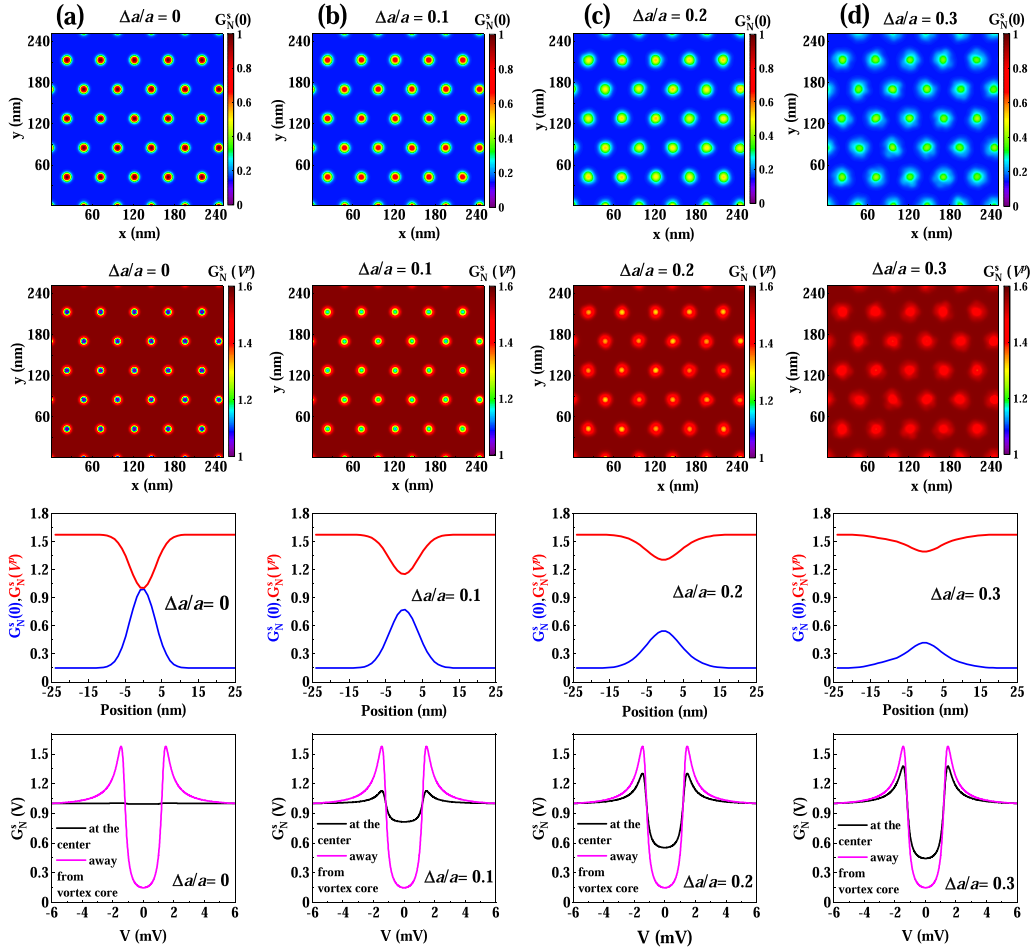
FIG. 3. Representative simulation of the normalized conductance at 10 kOe, 450 mK for different fluctuation amplitudes: (a) $\frac{\Delta a}{a} = 0$, (b) $\frac{\Delta a}{a} = 0.1$, (c) $\frac{\Delta a}{a} = 0.2$, and (d) $\frac{\Delta a}{a} = 0.3$. The top row shows the normalized conductance maps for $V = 0 [G_N^s(0) \equiv G_N^s(0, \mathbf{r}, \Delta a)]$. The second row shows the normalized conductance maps for $V = V^p = 1.45$ mV $[G_N^s(V^p) \equiv G_N^s(V^p, \mathbf{r}, \Delta a)]$. The third row shows the variation of $G_N^s(0)$ and $G_N^s(V^p)$ along a line passing through the center of the vortex. The bottom row shows the simulated $G_N(V)$ vs V spectra at the center of the vortex and at the midpoint of two vortices.

C. Fitting the experimental data and extracting the fluctuation amplitude

To fit the experimental data, we take $\Delta a/a$ and Γ as fitting parameters and constrain ξ within 25% of the value [22] obtained from $H_{c2}(\xi \approx 5.2\,\text{nm})$. Figures 4(a) and 4(b) show the line cuts of $G_N(0, r)$ along with the best fit $G_N^s(0, \mathbf{r}, \Delta a)$ at two different fields at 450 mK. (Fits for all magnetic field values are given in Appendix B). Above 10 kOe, we use a larger Γ than its zero-field value to account for the additional broadening from the orbital current around vortices. While we primarily analyze the variation of $G_N(0, r)$, we note that the same set of parameters reproduces the qualitative variation of $G_N(V^p, r)$, but the conductance value is overestimated by 15–20%; this is most likely due to the fact that the phenomenological Γ parameter does not capture suppression of the coherence peak from orbital supercurrent accurately. In Fig. 5(b), we plot $\Delta a/a$ as a function of magnetic field extracted at 450 mK. While Δa decreases with increasing field, $\Delta a/a$ shows an overall increasing trend. There are two anomalies observed close between 5–7 kOe and ~70 kOe,
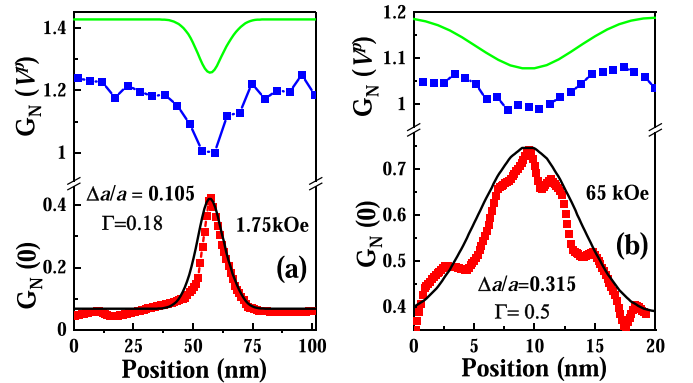

FIG. 4. (a) and (b) Spatial variation of $G_N(0)$ (red points) and $G_N(V^p)$ (blue points) along with corresponding theoretical fits (black and green lines) for two different magnetic fields; the spatial variation is obtained by averaging over three lines passing through the center of a vortex. The magnetic field value and the best fit values of $\frac{\Delta a}{a}$ and Γ corresponding to each panel are shown in the legend.
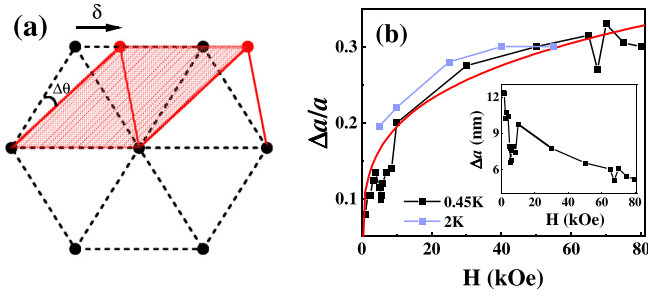
FIG. 5. (a) The black points show one undistorted hexagonal unit cell; the red points show the positions of the top two lattice points after applying a shear deformation (of exaggerated magnitude). The shaded red region shows the distorted primitive unit cell. (b) $\frac{\Delta a}{a}$ as a function of magnetic field at 450 mK (connected black points) and 2 K (connected blue points); the red line is a fit of the 450 mK data to $\frac{\Delta a}{a} \propto H^{\frac{1}{4}}$. The inset shows Δa as a function of field at 450 mK.

where we observe a sudden decrease. We will comment on this in the next subsection.

D. Theoretical analysis of vortex fluctuation

To quantitatively understand the magnetic field variation of $\Delta a/a$, we now theoretically compute this quantity within harmonic approximation. The lattice vibration of the 2D VL is governed by two elastic moduli [27,28]: compression C_{11} and shear C_{66}. However, $C_{66} \ll C_{11}$, and therefore, for small deformation, the elastic energy of the VL is mainly controlled by C_{66}. In the language of lattice vibrations, this means that transverse lattice vibration modes are easier to excite than longitudinal ones. Since the vortex motion is overdamped, we assume that each vortex oscillates individually. Therefore, instead of focusing on the full dispersion relation, we use a simple Einstein model of the VL phonon, as has been done in Ref. [15]. It is important to note that, even though this analysis is formulated assuming a vortex solid, it will remain valid even in a vortex fluid if there is short-range hexagonal coordination and if the timescale of diffusive motion of vortices is much larger than inverse of Einstein frequency

To start with, let us assume that vortices in a row are displaced by a distance δ ($\ll a$) from its equilibrium position, as shown in Fig. 5(a). The shear strain in the lattice is

$$\tan(\theta) \approx \theta = \frac{\delta}{a}. \tag{5}$$

The corresponding elastic energy per unit volume is

$$\varepsilon = \frac{1}{2} C_{66} \left(\frac{\delta}{a}\right)^2. \tag{6}$$

Thus, the total elastic energy per vortex $E = \varepsilon A d = \frac{1}{2} C_{66} (\frac{\delta}{a})^2 A d$, where A is area of rhombus unit cell, and d is the thickness of film. In the London limit, the shear modulus of an isotropic superconductor for small magnetic field is given by [27]

$$C_{66} = \frac{\Phi_0 H}{16\pi \mu_0 \lambda^2}. \tag{7}$$

Using this expression, the elastic energy is

$$E^{el} = \frac{\Phi_0 d}{32\pi \mu_0 \lambda^2} (HA) \left(\frac{\delta}{a}\right)^2 \tag{8}$$

Since we have one vortex per unit cell, $HA = \Phi_0$,

$$E^{el} = \frac{\Phi_0^2 d}{32\pi \mu_0 \lambda^2} \left(\frac{\delta}{a}\right)^2 = \frac{1}{2} \left(\frac{\Phi_0^2 d}{16\pi \mu_0 \lambda^2 a^2}\right) \delta^2. \tag{9}$$

Therefore, motion of vortices about their equilibrium positions is analogous to a harmonic oscillator with Einstein frequency

$$\omega = \sqrt{\frac{\Phi_0^2 d}{16\pi \mu_0 \lambda^2 a^2 m_v}} = \left(\frac{K}{m_v}\right)^{1/2} \frac{1}{a} = \omega_0 \left(\frac{H}{H_{c2}}\right)^{1/2}, \tag{10}$$

where m_v is vortex mass, $K = \frac{\Phi_0^2 d}{16\pi \mu_0 \lambda^2}$, and $\omega_0 = \frac{1}{1.075}(\frac{K H_{c2}}{m_v \Phi_0})^{1/2}$; we have used $a \approx 1.075(\frac{\Phi_0}{H})^{\frac{1}{2}}$ to get the last form.

The total energy for each vortex oscillating with amplitude Δa is given by the energy of the simple harmonic oscillator $m_v \omega^2 (\Delta a)^2$. To estimate the quantum zero-point motion, we equate this quantity to the zero-point energy $\hbar \omega$, which gives

$$\frac{\Delta a}{a} = \left[\frac{\hbar^{1/2}}{(K m_v)^{1/4}}\right] \left(\frac{1}{a}\right)^{1/2} \propto H^{1/4}. \tag{11}$$

This expression is very similar to a more detailed calculation in Ref. [16] and differs only by factor of 0.6 (see Appendix C). On the other hand, if the motion is thermal in origin, $m_v \omega^2 (\Delta a)^2 \approx k_B T$. In this case, $\frac{\Delta a}{a} \approx (\frac{k_B T}{K})^{1/2}$, which is independent of magnetic field.

In Fig. 5(b), we show the $\frac{\Delta a}{a}$ vs H variation at 450 mK and 2 K. We see that the $\frac{\Delta a}{a}$ vs H variation at 450 mK (black points) is very well captured with $H^{1/4}$ dependence (red line), consistent with quantum zero-point motion. From the coefficient of the fit and using the experimental value [22] of $\lambda \approx 534$ nm, we obtain $m_v \approx 36 m_e$ (where m_e is the electron mass). Though different estimates of m_v considerably vary [29–34], we can compare this value with the most widely used estimate [29] $m_v = \frac{2}{\pi^3} m^* k_F d$, where m^* is the effective mass, and k_F is the Fermi wave vector. Assuming $m^* = m_e$, and using the free electron expression $k_F = (3\pi^2 n)^{1/3}$, where $n = 5.2 \times 10^{29}$ el/m^3 is the carrier density determined from Hall effect, we obtain $m_v \approx 32 m_e$, which is in very good agreement with the value obtained from our experiments. On the other hand, the corresponding value of $\omega_0 = 8.65 \times 10^{11}$ Hz $< \Omega_0$, justifying the Born-Oppenheimer approximation used in Sec. IV B. Coming to the cusplike anomalies observed at between 5–7 kOe and 70 kOe, we note that these anomalies appear very close to the vortex solid-to-HVF and HVF-to-IVL boundaries, respectively. These anomalies most likely arise from the anharmonicity of the confining potential close to the phase boundaries, though a detailed understanding will require further investigations. It is interesting to note that the first anomaly appears when $\frac{\Delta a}{a} \approx 0.14$, which is in the ball-park value expected from the Lindemann criterion for melting.

Coming to the $\frac{\Delta a}{a}$ vs H data at 2 K, we note that the value is very close to the 450 mK value, for magnetic fields

>40 kOe but becomes larger than the 450 mK value at lower fields. To understand this behavior, we need to account for the role of thermal fluctuation. The quantum-to-thermal crossover is expected to happen when the thermal excitation energy exceeds the oscillator level spacing, i.e., $k_B T \gtrsim \hbar \omega = \hbar \omega_0 (\frac{H}{H_{c2}})^{1/2}$. Thus, at a given temperature, a simple estimate of this crossover field will be $H_{\mathrm{cross}} \approx H_{c2} (\frac{k_B T}{\hbar \omega_0})^2$; thermal and quantum fluctuations are expected to dominate for $H \ll H_{\mathrm{cross}}$ and $H \gg H_{\mathrm{cross}}$, respectively. At 450 mK, $H_{\mathrm{cross}} = 0.54$ kOe ($H_{c2} \approx 126$ kOe); since the lower limit of our data is 1 kOe, the magnetic field variation of $\frac{\Delta a}{a}$ can be understood based on quantum fluctuations alone. On the other hand, at 2 K, $H_{\mathrm{cross}} \approx 9.5$ kOe using the same value of ω_0 (since the λ does not change significantly in this temperature range) and $H_{c2} \approx 108$ kOe. Thus, for magnetic fields $\gg 9.5$ kOe, $\frac{\Delta a}{a}$ at 2K will be identical to 450 mK since both are governed by quantum fluctuations; as the field approaches 9.5 kOe, $\frac{\Delta a}{a}$ will become progressively larger due to the additional contribution from thermal fluctuations. This is qualitatively consistent with our data. However, a quantitative fit incorporating the combined effect of quantum and thermal fluctuations is beyond the scope of this paper.

V. CONCLUSIONS

We have shown evidence of quantum zero-point fluctuation of vortices at low temperatures in a 2D VL in a weakly pinned a-MoGe thin film. The spatial fluctuation of vortices leaves a very clear signature on the spectral property of the vortex in the form of a soft gap at the center of the vortex. Given the characteristic frequency of fluctuation from our analysis ($\omega_0 \approx 0.865$ THz), it might be worthwhile to look for direct signatures of vortex fluctuation from THz measurements. In this context, it is worthwhile to note that, in an earlier STS experiment on an Au(5 nm)/MoGe(20 nm) bilayer, it was observed that, on the Au surface, the minigap induced by the underlying MoGe does not go to zero at the center of a vortex [35]. This could be for the same reason as that described in this paper, even though, in that experiment, proximity effect is likely to give an additional contribution. It would also be interesting to investigate the impact of zero-point fluctuations on the state of the 2D VL at low temperatures. In liquid ^{4}He, the zero-point fluctuation prevents the liquid from solidifying and thus producing a quantum fluid at $T = 0$. Whether zero-point fluctuations can produce a quantum vortex fluid at very low temperatures is at present unclear. Even though existing studies indicate that the hexatic and isotropic vortex fluid continue to exist over a large magnetic field range down to 450 mK, it would be interesting to explore this more carefully through transport and STS imaging down to lower temperatures.

S.D. and I.R. performed the STS measurements and analyzed the data. J.J. optimized deposition conditions and synthesized the samples. The theoretical analyses were carried out by S.D., S.S., and P.R., P.R. conceived the problem, supervised the experiments, and wrote the paper. All authors read the manuscript and commented on the paper.

APPENDIX A: SIMULATING THE CONDUCTANCE MAP FOR A VL

To cross-check the validity of the phenomenological model used to simulate the conductance maps for a VL, we apply it to a conventional system, namely, the vortex state in clean 2H-NbSe$_2$ (single crystal), where we do not have any evidence that the vortices fluctuate about their mean positions. Figure 6(a) shows the VL image on a NbSe$_2$ single crystal at 5 kOe, 450 mK, keeping the bias voltage at 1.2 meV, close to the coherence peak. Figure 6(b) shows the $G_N(V)$ vs V spectra along a line passing through the center of the vortex. Here, the core of vortex shows a zero-bias conductance peak [$G_N(V = 0) > 1$] resulting from the bound state of normal electrons inside the normal core, known as a CdGM bound state [3]. On the other hand, spectra obtained at superconducting regions away from the VC have regular BCS characteristics, partially broadened by the circulating current around the VC [inset, Fig. 6(c)]. The experimental variation of $G_N(0)$ along three lines passing through the center of the vortex as well as their average is shown in Fig. 6(c).

The VL is simulated as follows. We assume that far away from the VC $G_N(V)$ will be like the conductance spectra in zero field. This is obtained by fitting the zero-field experimental tunneling conductance with BCS theory using superconducting energy gap Δ and phenomenological broadening parameter Γ as the fitting parameters; we call this resultant best fit spectrum as $G_N^{\mathrm{BCS}}(V)$. For the spectra at the center at the vortex center $G_N^{\mathrm{center}}(V)$, we used the average of the experimental spectra obtained at the center of the several vortices. These two spectra are shown in Fig. 6(d). To interpolate between these two, we use an empirical Gaussian weight factor $f(\mathbf{r}) = \exp(-\frac{r^2}{2\sigma^2})$, such that $G_N(V, \mathbf{r}) = f(\mathbf{r}) G_N^{\mathrm{center}}(V) + [1 - f(\mathbf{r})] G_N^{\mathrm{BCS}}(V)$, where $\mathbf{r}$ is the position with respect to the center of the vortex. We choose $\sigma \approx \xi$, where $\xi \approx 8.9$ nm (corresponding to the measured $H_{c2} \approx 42$ kOe) is the Ginzburg-Landau coherence length of clean NbSe$_2$. Using this, we construct the VL by linear superposition of conductance values from all vortices and henceforth obtain a resultant conductance map given by $\tilde{G}_N(V, \mathbf{r}) = 1.6 \sum_i G_N(V, \mathbf{r} - \mathbf{r}_i) / [\sum_i G_N(V = 0, \mathbf{r} - \mathbf{r}_i)]_{\mathrm{max}}$, where the position of ith vortex is $\mathbf{r}_i$. This construct ensures that, at the center of the vortex, the simulated conductance matches with the experimental zero-bias conductance at the vortex center. In Fig. 6(e), we compare the experimental variation of $G_N(0)$ for a line passing through the vortex center along with the corresponding value obtained from our simulation. The inset shows the corresponding data for $G_N(V^p = 1.2$ meV), which is close to the superconducting coherence peaks. The good agreement in both cases shows the validity of our phenomenological approach to simulate the conductance map.
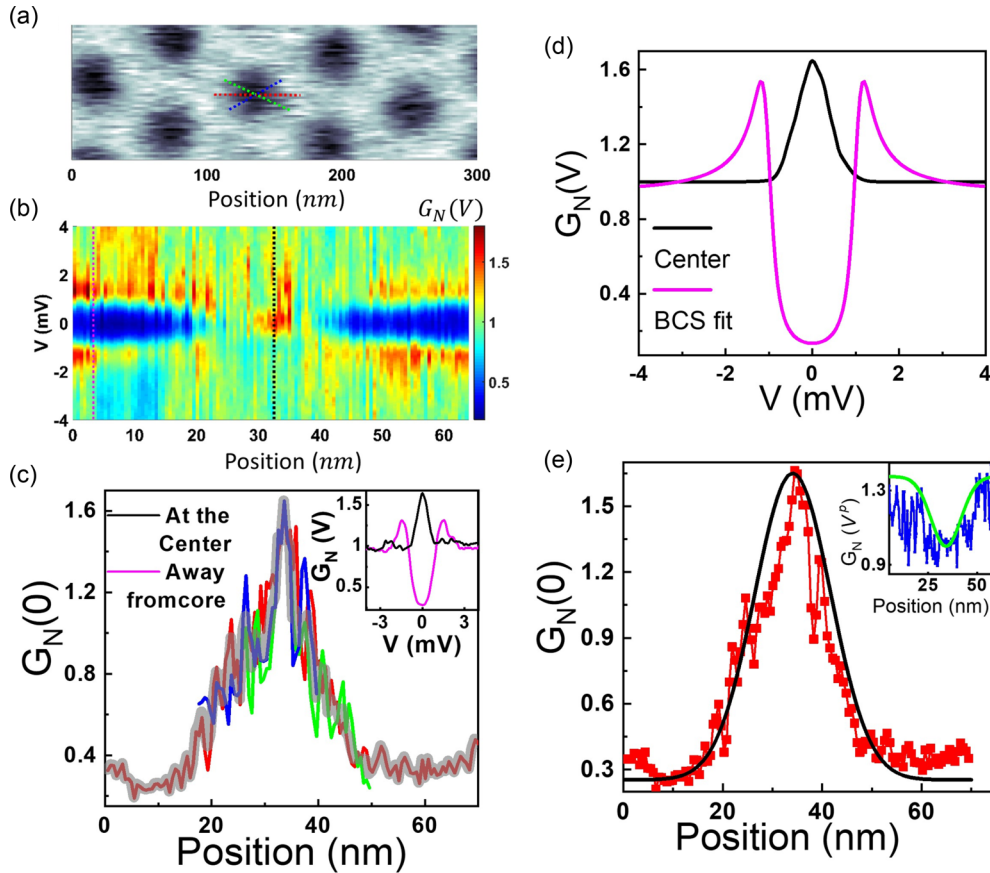
FIG. 6. (a) Vortex image on NbSe$_2$, observed by recording $\Delta G(V = 1.2$ meV) across the area, showing three lines passing through a vortex center. (b) $G_N(V)$ vs V spectra along the red dotted line in (a) with black dotted line denoting the center of the vortex. (c) Variation of $G_N(0)$ along the dotted lines passing through the vortex cores (VCs) in (a); inset: two spectra at the black and pink dotted lines in (b), respectively. The transparent gray is the average of the three. (d) The two spectra at the center of the VC and far away from the VC taken for the purpose of our simulation. (e) Simulated $G_N(0)$ (black line) along with the average $G_N(0)$ (red squares) for three lines passing through the center of the vortex obtained from experimental data. (inset) Simulated $\tilde{G}_N(V = 1.2$ meV) (green line) along with the average $G_N(V = 1.2$ meV) (blue line) obtained from experimental data.

One difference between the above simulation and the one in the case in *a*-MoGe is that, in that case, we take $G_N^{\text{center}}(V) = 1$. The reason is that the zero-bias conductance peak at the center of the VC is very sensitive to disorder, and a very small amount of scattering (such as a small amount of Co doping in NbSe$_2$) destroys the peak, giving a flat spectrum [36]. Therefore, it is unlikely to be present even in the absence of fluctuations in *a*-MoGe, where the electronic mean free path is very small due to the amorphous nature of the sample.

APPENDIX B: FIT OF THE $G_N(0)$ PROFILE PASSING THROUGH THE VC

In Fig. 4, we show two representative fits of our model with $G_N(0)$ profiles passing through the VC. In Figs. 7(a)–7(h), we show the fits at several other magnetic fields (at 450 mK), along with the best fit parameters. Figure 7(i) shows the value of Γ used to fit the profiles. Above 10 kOe, we need to gradually increase the value of Γ to consider the broadening arising from orbital current around the VC.

APPENDIX C: COMPARISON BETWEEN EQ. (11) AND THE EXPRESSION DERIVED IN REF. [16]

In this section, we will provide a detailed calculation to show that the expression of $\Delta a/a$, given by Eq. (11) is like the expression derived in Ref. [16]. We start with eqn. 33 of Ref. [16], which in the harmonic limit reduces to

$$m_v = \frac{0.03627 a_v^2 \hbar^2}{\rho_s u_{\text{rms}}^4}, \tag{C1}$$

where $a_v \equiv a$ is the separation between nearest neighbor vortices, and u_{rms}^2 is the mean square displacement. Here, ρ_s is the superfluid stiffness, and it is denoted as

$$\rho_s = \frac{\hbar^2 c^2 d}{16\pi e^2 \lambda^2} = \frac{\hbar^2 d}{4\mu_0 e^2 \lambda^2} = \frac{4}{\pi} K. \tag{C2}$$

From Eq. (C1), we get

$$u_{\text{rms}}^4 = \frac{0.03627 a_v^2 \hbar^2}{\rho_s m_v} \Rightarrow \frac{u_{\text{rms}}}{a_v} = \left(\frac{0.03627 \hbar^2}{\rho_s m_v}\right)^{1/4} \frac{1}{\sqrt{a_v}}. \tag{C3}$$
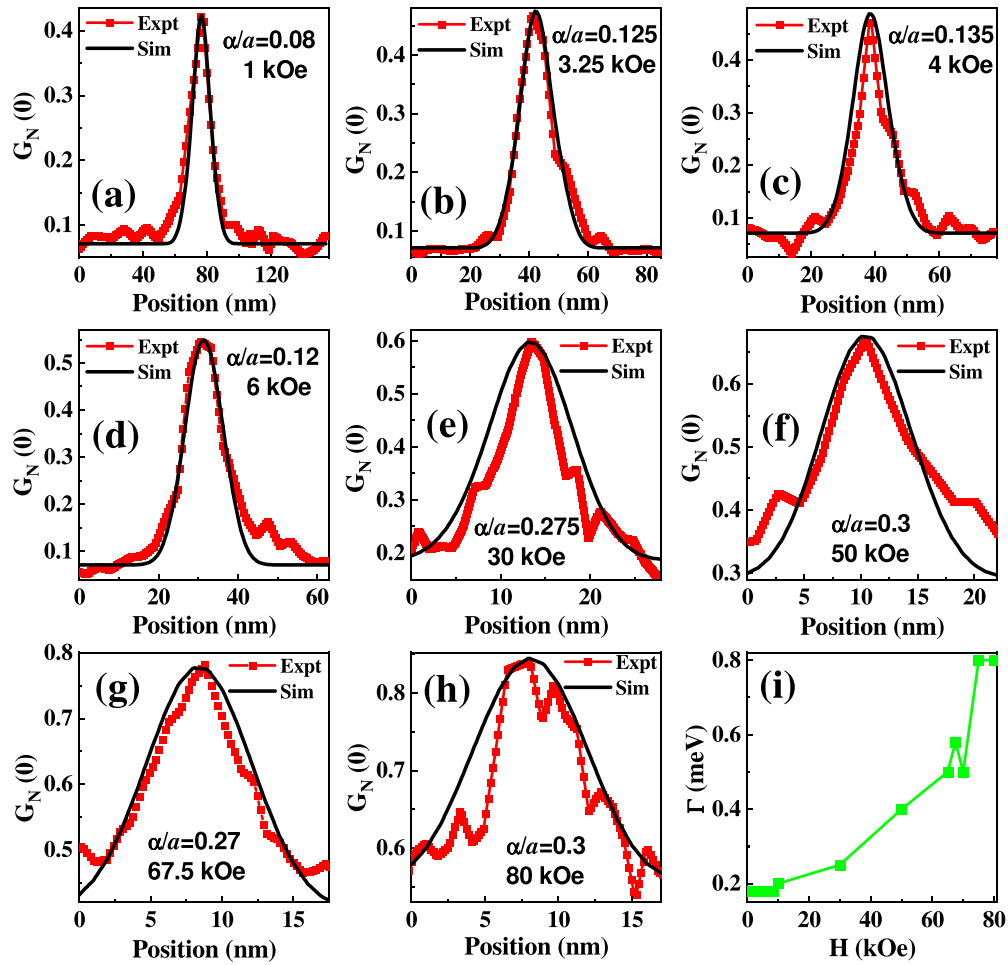
FIG. 7. (a)–(h) The red connected points are averaged line cuts of $G_N(0, r)$ passing through the center of a vortex core in different magnetic fields. The black lines are line cuts of simulated $G_N^s(0, r)$ at the corresponding field. (i) Magnetic field variation of the broadening parameter Γ used in the fits.

Now using Eq. (C2) and noting that the amplitude of oscillation ($\Delta a = \sqrt{2} u_{\mathrm{rms}}$), we can write Eq. (C3) as

$$\frac{\Delta a}{a} = \sqrt{2}\left(\frac{0.03627 \hbar^2}{\frac{4}{\pi} K m_v}\right)^{1/4}\left(\frac{1}{a}\right)^{1/2} = 0.6 \frac{\hbar^{1/2}}{(K m_v)^{1/4}}\left(\frac{1}{a}\right)^{1/2}. \quad (C4)$$

Equation (C4) identical to Eq. (11) except for the factor of 0.6.

[1] M. Tinkham, *Introduction to Superconductivity*, 2nd ed. (McGraw-Hill, New York, 1996).

[2] J. Bardeen and M. J. Stephen, Theory of the motion of vortices in superconductors, Phys. Rev. **140**, A1197 (1965).

[3] C. Caroli, P. G. de Gennes, and J. Matricon, Bound fermion states on a vortex line in a type II superconductor, J. Phys. Lett. **9**, 307 (1964).

[4] H. F. Hess, R. B. Robinson, and J. V. Waszczak, Vortex-Core Structure Observed with a Scanning Tunneling Microscope, Phys. Rev. Lett. **64**, 2711 (1990).

[5] M. Chen, X. Chen, H. Yang, Z. Du, X. Zhu, E. Wang, and H. Wen, Discrete energy levels of Caroli–de Gennes–Matricon

states in quantum limit in FeTe$_{0.55}$Se$_{0.45}$, Nat. Commun. **9**, 970 (2018).

[6] C. Chen, Q. Liu, W-C. Bao, Y. Yan, Q-H. Wang, T. Zhang, and D. Feng, Observation of Discrete Conventional Caroli–de Gennes–Matricon States in the Vortex Core of Single-Layer FeSe/SrTiO₃, Phys. Rev. Lett. **124**, 097001 (2020).

[7] Ch. Renner, A. D. Kent, Ph. Niedermann, and Q. Fischer, Scanning Tunneling Spectroscopy of a Vortex Core from the Clean to the Dirty Limit, Phys. Rev. Lett. **67**, 1650 (1991).

[8] E. Herrera, I. Guillamón, J. A. Galvis, A. Correa, A. Fente, R. F. Luccas, F. J. Mompean, M. García-Hernández, S. Vieira, J. P. Brison, and H. Suderow, Magnetic field dependence of

the density of states in the multiband superconductor β-Bi$_2$Pd, Phys. Rev. B **92**, 054507 (2015).

[9] Ch. Renner, B. Revaz, K. Kadowaki, I. Maggio-Aprile, and Ø. Fischer, Observation of the Low Temperature Pseudogap in the Vortex Cores of Bi$_2$Sr$_2$CaCu$_2$O$_{8-\delta}$, Phys. Rev. Lett **80**, 3606 (1998).

[10] J. Bruér, I. Maggio-Aprile, N. Jenkins, Z. Ristić, A. Erb, C. Berthod, Ø. Fischer, and C. Renner, Revisiting the vortex-core tunnelling spectroscopy in YBa$_2$Cu$_3$O$_{7-\delta}$, Nat. Commun. **7**, 11139 (2016).

[11] Y. Noat, V. Cherkez, C. Brun, T. Cren, C. Carbillet, F. Debontridder, K. Ilin, M. Siegel, A. Semenov, H.-W. Hübers, and D. Roditchev, Unconventional superconductivity in ultra-thin superconducting NbN films studied by scanning tunneling spectroscopy, Phys. Rev. B **88**, 014503 (2013).

[12] R. Ganguly, I. Roy, A. Banerjee, H. Singh, A. Ghosal, and P. Raychaudhuri, Magnetic field induced emergent inhomogeneity in a superconducting film with weak and homogeneous disorder, Phys. Rev. B **96**, 054509 (2017).

[13] A. Datta, A. Banerjee, N. Trivedi, and A. Ghosal, New paradigm for a disordered superconductor in a magnetic field, arXiv:2101.00220.

[14] H. J. Fink, Vortex Wave Spectrum of a Type II Superconductor, Phys. Rev. Lett. **12**, 578 (1964).

[15] L. Bartosch and S. Sachdev, Influence of the quantum zero-point motion of a vortex on the electronic spectra of s-wave superconductors, Phys. Rev. B **74**, 144515 (2006).

[16] L. Bartosch, L. Balents, and S. Sachdev, Detecting the quantum zero-point motion of vortices in the cuprate superconductors, Ann. Phys. **321**, 1528 (2006).

[17] I. Roy, S. Dutta, A. N. Roy Choudhury, S. Basistha, I. Maccari, S. Mandal, J. Jesudasan, V. Bagwe, C. Castellani, L. Benfatto, and P. Raychaudhuri, Melting of the Vortex Lattice through Intermediate Hexatic Fluid in an a-MoGe Thin Film, Phys. Rev. Lett. **122**, 047001 (2019).

[18] S. Dutta, I. Roy, S. Basistha, S. Mandal, J. Jesudasan, V. Bagwe, and P. Raychaudhuri, Collective flux pinning in hexatic vortex fluid in a-MoGe thin film, J. Phys.: Condens. Matter **32**, 075601 (2020).

[19] S. Dutta, I. Roy, S. Mandal, J. Jesudasan, V. Bagwe, and P. Raychaudhuri, Extreme sensitivity of the vortex state in a-MoGe films to radio-frequency electromagnetic perturbation, Phys. Rev. B **100**, 214518 (2019).

[20] A. Kamlapure, G. Saraswat, S. C. Ganguli, V. Bagwe, P. Raychaudhuri, and S. P. Pai, A 350 mK, 9 T scanning tunnelling microscope for the study of superconducting thin films on insulating substrates and single crystals, Rev. Sci. Instrum. **84**, 123905 (2013).

[21] R. C. Dynes, V. Narayanamurti, and J. P. Garno, Direct Measurement of Quasiparticle-Lifetime Broadening in a Strong-Coupled Superconductor, Phys. Rev. Lett. **41**, 1509 (1978).

[22] S. Mandal, S. Dutta, S. Basistha, I. Roy, J. Jesudasan, V. Bagwe, L. Benfatto, A. Thamizhavel, and P. Raychaudhuri, Destruction of superconductivity through phase fluctuations in ultrathin a-MoGe films, Phys. Rev. B **102**, 060501(R) (2020).

[23] K. D. Usadel, Generalized Diffusion Equation for Superconducting Alloys, Phys. Rev. Lett. **25**, 507 (1970).

[24] M. Amundsen and J. Linder, General solution of 2D and 3D superconducting quasiclassical systems: Coalescing vortices and nanoisland geometries, Sci. Rep. **6**, 22765 (2016).

[25] M. R. Eskildsen, M. Kugler, S. Tanaka, J. Jun, S. M. Kazakov, J. Karpinski, and Ø. Fischer, Vortex Imaging in the π Band of Magnesium Diboride, Phys. Rev. Lett. **89**, 187003 (2002).

[26] A. Fente, E. Herrera, I. Guillamón, H. Suderow, S. Mañas-Valero, M. Galbiati, E. Coronado, and V. G. Kogan, Field dependence of the vortex core size probed by scanning tunneling microscopy, Phys. Rev. B **94**, 014517 (2016).

[27] E. H. Brandt, The vortex lattice in conventional and high-T_c superconductors, Braz. J. Phys. **32**, 675 (2002).

[28] G. J. C. van Baarle, F. Galli, P. H. Kes, and J. Aarts, Vortex relaxation and coupling in superconducting heterostructures studied by STM, arXiv:cond-mat/0702106.

[29] H. Suhl, Inertial Mass of a Moving Fluxoid, Phys. Rev. Lett. **14**, 226 (1965).

[30] E. M. Chudnovsky and A. B. Kuklov, Inertial Mass of the Abrikosov Vortex, Phys. Rev. Lett. **91**, 067004 (2003).

[31] N. B. Kopnin and V. M. Vinokur, Dynamic Vortex Mass in Clean Fermi Superfluids and Superconductors, Phys. Rev. Lett. **81**, 3952 (1998).

[32] M. W. Coffey, On the inertial mass of a vortex in high-T_c superconductors: Closed form results, J. Phys. A: Math. Gen. **31**, 6103 (1998).

[33] E. Šimánek, Inertial mass of a fluxon in a deformable superconductor, Phys. Lett. A **154**, 309 (1991).

[34] D. M. Gaitonde and T. V. Ramakrishnan, Inertial mass of a vortex in cuprate superconductors, Phys. Rev. B **56**, 11951 (1997).

[35] R. Panghotra, M. Timmermans, C. Xue, B. Raes, V. Moshchalkov, and J. Van de Vondel, Exploring the impact of core expansion on the vortex distribution in superconducting–normal-metal hybrid nanostructures, Phys. Rev. B **100**, 054519 (2019).

[36] S. C. Ganguli, H. Singh, R. Ganguly, V. Bagwe, A. Thamizhavel, and P. Raychaudhuri, Orientational coupling between the vortex lattice and the crystalline lattice in a weakly pinned Co$_{0.0075}$NbSe$_2$ single crystal, J. Phys.: Condens. Matter **28**, 165701 (2016).